Structure of the photosynthetic Calvin-Benson-Bassham sedoheptulose-1,7-bisphosphatase SBPase from the model microalga *Chlamydomonas reinhardtii*

Théo Le Moigne[1,2], Martina Santoni[1,3], Lucile Jomat[1], Stéphane D. Lemaire[1], Mirko Zaffagnini[3], Nicolas Chéron[4], Julien Henri[1,*]

1. Sorbonne Université, CNRS, Laboratoire de Biologie Computationnelle et Quantitative UMR 7238, Institut de Biologie Paris-Seine, 4 Place Jussieu, Paris F-75005, France

2. Faculty of Sciences, Doctoral School of Plant Sciences, Université Paris-Saclay, Saint-Aubin F-91190, France

3. Department of Pharmacy and Biotechnology, University of Bologna, Via Irnerio 42, Bologna I-40126, Italy

4. Ecole Normale Supérieure, CNRS, Sorbonne Université, Laboratoire Pasteur UMR 8640, Département de Chimie de l'Ecole Normale Supérieure rue d'Ulm, F-Paris 75005, France

*corresponding author

e-mail: julien.henri@sorbonne-universite.fr

Phone: +33144276606

ORCID: Théo Le Moigne 0000-0003-2313-3052; Stéphane Lemaire 0000-0001-6442-0547, Mirko Zaffagnini 0000-0001-5115-0859, Nicolas Chéron 0000-0002-4090-5897; Julien Henri 0000-0003-0772-8881

Abstract

The Calvin-Benson-Bassham cycle (CBBC) performs carbon fixation in photosynthetic organisms. Among the eleven enzymes that participate in the pathway, sedoheptulose-1,7-bisphosphatase (SBPase) is expressed in photo-autotrophs and contributes to the regeneration of ribulose-1,5-bisphosphate, the carbon fixation co-substrate used by ribulose-1,5-bisphosphate carboxylase/oxygenase (Rubisco). While SBPase is structurally similar to fructose-1,6-bisphosphatase (FBPase) involved in both neoglucogenesis and the CBBC, it exclusively functions in the CBBC and is indispensable for building a productive cycle. In this study we report the first structure of an SBPase from a chlorophyte, the model unicellular green microalga *Chlamydomonas reinhardtii*. By combining experimental and computational structural analyses, we describe the topology, conformations and quaternary structure of *Chlamydomonas reinhardtii* SBPase. We identify active site residues and locate sites of redox- and phospho-post-translational modifications that contribute to enzymatic functions. Finally, we observe that *Cr*SBPase adopts distinct oligomeric states that may dynamically contribute to the control of its activity.

Introduction

Photosynthetic carbon fixation is performed by eleven enzymes that collectively operate the Calvin-Benson-Bassham cycle (CBBC) (Calvin 1962, Johnson 2016), wherein Rubisco plays the prominent role in catalyzing fixation of inorganic carbon onto a pentose acceptor: ribulose-1,5-bisphosphate (RuBP). The net gain of the CBBC is one triose in the form of glyceraldehyde-3-phosphate (G3P) for every three Rubisco catalyzed carboxylation reactions (Johnson and Alric 2013). Regeneration of RuBP is ensured by the other ten enzymes of the CBBC, among which phosphoribulokinase (PRK) catalyzes the phosphorylation of ribulose-5-phosphate (R5P) and sedoheptulose-1,7-bisphosphatase (SBPase) catalyzes the hydrolysis of sedoheptulose-1,7-bisphosphate (SBP) into sedoheptulose-7-phosphate (S7P). Remaining CBBC enzymes are paralogs of those involved in cytoplasmic glycolysis, neoglucogenesis or the pentose-phosphate pathway. Hence, Rubisco, PRK, and SBPase are expressed

51 in photosynthetic organisms and fulfil biochemical functions so far uniquely attributed to the
52 photosynthetic CBBC. The CBBC is perfectly conserved in plants and cyanobacteria since its enzymes
53 are expressed in oxygenic prokaryotes and plant chloroplasts, which consist in subcellular
54 compartments that evolved from ancestral endosymbiosis between cyanobacteria and heterotrophic
55 eukaryotic cells. For instance, the analysis of PRK from *Synechococcus* PCC 6301, *Arabidopsis*
56 *thaliana*, and *Chlamydomonas reinhardtii* display high structural similarities (Gurrieri, Del Giudice et
57 al. 2019, Wilson, Hayer-Hartl et al. 2019).
58 Native SBPase was purified from wheat chloroplasts (Woodrow 1982) and corn leaves (Nishizawa and
59 Buchanan 1981), allowing quantitative assays of its catalytic function and the *in vitro* confirmation of
60 magnesium-dependent activation and activity modulation by pH and redox switch mechanisms
61 (Anderson 1974, Woodrow and Walker 1980, Cadet and Meunier 1988). Redox control is exerted
62 through a dithiol/disulfide interchange dependent upon the ferredoxin-thioredoxin cascade arising
63 from the activity of the illuminated photosystems (Schürmann and Buchanan 1975). In tobacco
64 leaves extracts, SBPase reaches its maximal activity after 10 minutes illumination (Zimmer, Swart et
65 al. 2021). This delayed activation kinetics is consistent with the slow reduction pattern of *Arabidopsis*
66 SBPase *in vitro* (Yoshida and Hisabori 2018).
67 The crystal structure of SBPase from the moss *Physcomitrium patens* (*Pp*SBPase) has been solved at a
68 resolution of 1.3 Å (Protein Data Bank entry : 5iz3) (Gutle, Roret et al. 2016). *Pp*SBPase fold is highly
69 similar to that of moss FBPase, yet the protein was shown to distinctively oligomerize as a
70 homodimer and to form a disulfide bridge in a different motif than that previously described for
71 FBPase (Chiadmi, Navaza et al. 1999). In spite of their homology, the sequences of FBPase and
72 SBPase seem to have evolved different regulatory properties that allow different contributions to the
73 CBBC. Recently, it was proposed that the CBBC can bypass fructose-1,6-bisphosphate (FBP)
74 altogether, by only relying on SBP, glycolysis and the oxidative pentose-phosphate pathway paralogs
75 to regenerate the substrate of Rubisco (Ohta 2022). Engineered SBPase overexpression enhances
76 photosynthesis and growth in plants (Lefebvre, Lawson et al. 2005, Feng, Han et al. 2007, Feng, Wang

77 et al. 2007, Rosenthal, Locke et al. 2011, Simkin, Lopez-Calcagno et al. 2017) and in the green
78 microalga *Chlamydomonas reinhardtii* (Hammel, Sommer et al. 2020), indicating that SBPase appears
79 as a metabolic bottleneck for the CBBC along with Rubisco. Based on these evidences, it is plausible
80 to consider that SBPase is a good target to improve the photosynthetic capacity by means of
81 metabolic engineering coupled to synthetic biology (Kubis and Bar-Even 2019), especially in the
82 experimentally convenient multi-omic model alga Chlamydomonas (Mettler, Muhlhaus et al. 2014,
83 Schmollinger, Mühlhaus et al. 2014).
84 In Chlamydomonas, SBPase is encoded by a single nuclear gene (Cre03.g185550), and the protein
85 (Uniprot entry P46284) is addressed to the chloroplast by a 54-residue amino-terminal peptide
86 (Emanuelsson, Brunak et al. 2007, Almagro Armenteros, Salvatore et al. 2019). SBPase abundance in
87 the algal cell was quantified by mass spectrometry as 1.1-1.3 ± 0.3 amol/cell, representing 0.15 % of
88 total cell proteins (Hammel, Sommer et al. 2020). In Chlamydomonas protein extracts, SBPase was
89 shown to undergo post-translational modifications by phosphorylation of serines and threonines
90 (Werth, McConnell et al. 2017), and redox modifications of cysteine thiols (Zaffagnini, Bedhomme et
91 al. 2012, Morisse, Zaffagnini et al. 2014, Pérez-Pérez, Mauriès et al. 2017). However, the mechanisms
92 by which post-translational modifications affect the catalytic activity of CrSBPase is still lacking. Here,
93 we describe the crystal structures of *Cr*SBPase in two redox states, assay its activity *in vitro*, and
94 investigate the correlation between the redox state and the oligomerization of the protein. Our
95 results suggest that a redox control over oligomer equilibrium could represent a novel mechanism to
96 regulate enzymatic activities in the CBBC.
97

98 **Material and methods**

99 Chemical reagents were purchased from Merck (Darmstadt, Germany), chromatography material
100 was provided by Cytiva (Vélizy-Villacoublay, France), crystallization solutions and consumable were
101 purchased from Qiagen (Hilden, Germany), Hampton Research (Aliso Viejo, CA USA), and SPT Labtech
102 (Melbourn, UK).

103

104 **Cloning and mutagenesis of *Cr*SBPase expression plasmids**

105 The sequence coding for full-length mature SBPase was amplified by reverse transcriptase
106 polymerase chain reaction (RT-PCR) from *Chlamydomonas reinhardtii* total ribonucleic acids extract
107 and inserted at sites 5'-NdeI and BamHI-3' into expression vector pET3c modified for the fusion of an
108 amino-terminal hexa-histidine tag in the recombinant protein, yielding plasmid pSL-175-His_6-
109 *Cr*SBPase-WT. PCR primers were 5'-TCTCGCCATATGGCCGTTCTGACCCAGGCC-3' (forward, NdeI site
110 underlined) and 5'-CGGGTGGGATCCTTAGGCAGCCACCTTCTC-3' (reverse, BamHI site underlined). The
111 encoded protein encompasses 331 amino acids, with a molar mass of 36,176.7 Da and a theoretical
112 extinction coefficient of 24,722.5 $M^{-1}.cm^{-1}$. Unless otherwise stated, amino acid residues numbering
113 is that of GenBank entry DAA79954.1. Point mutants of cysteines 115 and 120 singly substituted with
114 serines were generated by site-directed PCR mutagenesis with primers listed in supplementary table
115 1, producing plasmids pSL-181-His6-*Cr*SBPase-C115S, and pSL-182-His6-*Cr*SBPase-C120S.

116

117 **Recombinant *Cr*SBPase purification**

118 Plasmids pSL-175, -181, and -182 were used to transform *Escherichia coli* BL21(DE3). The
119 transformants were grown at 37 °C in 2YT supplemented with 150 µg/mL ampicillin. When cultures
120 reached an OD_{600} of ~0.6, T7-dependent *Cr*SBPase overexpression was induced by the addition of
121 isopropyl-β-D-thiogalactopyranoside (IPTG) at 0.2 mM for 3 h.

122 Harvested cell pellets were resuspended in 20 $mmol.L^{-1}$ Tris pH 7.9, 100 $mmol.L^{-1}$ NaCl (buffer A) and
123 lyzed by 1 sec / 1 sec pulsed sonication for 3 min. The soluble fraction of the lysate was separated by
124 20 min centrifugation at 20,000 *g* and loaded on 2 mL Ni-NTA resin for His-tag mediated affinity
125 chromatography. The resin was washed in four steps with 25 mL buffer A, 25 mL buffer A
126 supplemented with 10, 20, and 30 $mmol.L^{-1}$ imidazole, and *Cr*SBPase was eluted with 10 mL buffer A
127 supplemented with 100, 200, and 300 $mmol.L^{-1}$ imidazole. Pooled eluates containing *Cr*SBPase were
128 loaded on HiLoad Superdex 200 26/600 size-exclusion chromatography column and eluted in buffer

129 A. Protein purity was assessed by electrophoresis on 12% acrylamide gel under denaturing and
130 reducing conditions (supplementary figure 1). Peak fractions were assembled and concentrated by
131 ultrafiltration on Amicon units of MWCO 30,000 Da cut-off. Final concentrations of purified proteins
132 were in the 1-10 $mg.mL^{-1}$ range as measured by Nanodrop ND-2000 spectrophotometer.
133
134 **Western blot**
135 Polyclonal antibodies were generated by immunization of rabbits with pure recombinant *Cr*SBPase
136 (Genecust, Boynes France). Analyzed fractions were separated by denaturing polyacrylamide
137 electrophoresis and transferred to nitrocellulose membrane for detection with primary antibody
138 subsequently detected by secondary anti-rabbit antibodies coupled to horseradish peroxidase.
139 Detection was done with commercial ECL peroxidase assay (GE Healthcare, Chicago IL USA) with a
140 Chemidoc (Bio-Rad, Hercules CA USA).
141
142 **Crystallization and structure determination**
143 Pure recombinant His6-*Cr*SBPase-WT concentrated at 3-6 mg/mL was tested for crystallization on
144 screens JCSG I-IV in 200 nL sitting drops. Single crystals were obtained and optimized with mother
145 liquor 0.1 $mol.L^{-1}$ sodium HEPES pH=7.5, 2% (v/v) polyethylene glycol 400, 2.0 $mol.L^{-1}$ ammonium
146 sulfate, flash-frozen in mother liquor supplemented with 25% glycerol and tested for X-ray
147 diffraction. Complete X-ray diffraction datasets were collected at SOLEIL beamline Proxima-2A and
148 allowed the determination of the crystal structure by model replacement with 5iz3, the structure of
149 ortholog SBPase from the moss *Physcomitrium patens.* Model building in COOT and refinement in the
150 PHENIX software suite yielded structure 7b2o (Emsley, Lohkamp et al. 2010) (Adams, Afonine et al.
151 2011) (Liebschner, Afonine et al. 2019). After we obtained our experimental structure, the European
152 Bioinformatics Institute (Hinxton, UK) communicated high-accuracy prediction models computed by
153 Deepmind ALPHAFOLD2 (Jumper, Evans et al. 2021), including a prediction of *Cr*SBPase structure
154 (https://alphafold.ebi.ac.uk/entry/P46284) that matches 7b2o crystal structure with RMSD=0.453 Å.

155 Hence, X-ray crystallography and ALPHAFOLD independently contribute to the proposed structural
156 analysis.
157 In order to determine the structure of *Cr*SBPase in a reduced state, crystals were grown in the
158 presence of 10 mmol.L^{-1} of the reducing agent tris-(2-carboxyethyl)phosphine (TCEP) in condition
159 JCSG IV E8/56 0.2 M lithium sulfate, 0.1 M Tris pH 7.0, 1.0 M sodium/potassium tartrate. Crystals
160 were cryo-protected in mother liquor supplemented with 25% ethylene glycol, flash-frozen and
161 tested for X-ray diffraction at SOLEIL beamline Proxima-2A. A complete dataset was collected that
162 allowed the determination of the structure by molecular replacement with 7b2o as a template.
163 Among the eight *Cr*SBPase copies of the asymmetric unit, two had their disulfides absent as a
164 consequence of the TCEP treatment while the others six subunits were essentially identical to
165 untreated structures in entry 7b2o.
166
167 **Enzymatic assays**
168 The catalytic activity of 10-200 nmol.L^{-1} pure recombinant *Cr*SBPase was spectrophotometrically
169 assayed in buffer A by coupling the hydrolysis of 1 M fructose-1,6-bisphosphate (FBP) into fructose-6-
170 phosphate (F6P) to the reduction of 0.5 M $NADP^+$ into NADPH through isomerization of F6P into
171 glucose-6-phosphate (G6P) by 0.5 U.mL^{-1} phosphoglucose isomerase (PGI) and the oxidation of G6P
172 into 6-phosphogluconolactone (6PGL) by 0.1-0.5 U.mL^{-1} glucose-6-phosphate dehydrogenase
173 (G6PDH). Reporter assay is coupled in a molar ratio FBP:F6P:G6P:6PGL of 1:1:1:1 to the oxidation of
174 one molar equivalent of $NADP^+$ into NADPH that we recorded over 0-20 minutes by measuring the
175 absorbance at 340 nm using a UVIKON spectrophotometer. Pre-treatment with 0-100 mmol.L^{-1} DTT,
176 0-30 mmol.L^{-1} $MgSO_4$, and 0-15 µmol.L^{-1} recombinant *Cr*TRX-f2 supplemented with 1 mM DTT
177 (Lemaire, Tedesco et al. 2018) was carried out for 30 min at room temperature before adding the
178 enzyme in the assay solution.
179

180 **Titration of accessible cysteine thiols**

181 Quantification of free reactive cysteines on recombinant CrSBPase was performed with 5,5′-dithio-
182 bis-(2-nitrobenzoic acid) (DTNB, Ellman's reagent) mixed with the purified recombinant protein in a
183 200:1 molar ratio in a 1 mL reaction volume containing 100 mM Tris-HCl, pH 7.9. Reaction of DTNB
184 with solvent-exposed cysteine thiols produces 2-nitro-5-thiobenzoate (TNB^-) that we quantified by
185 monitoring the absorbance at 412 nm and a molar extinction coefficient of TNB^- of 14.15 $mM^{-1}.cm^{-1}$.
186 We calculated the number of free reactive cysteines per *Cr*SBPase monomer by dividing the molar
187 concentration of TNB^- by that of the protein at equilibrium (t >60 min).

188

189 **Molecular dynamics**

190 Molecular dynamics (MD) simulations were performed with the Gromacs package (v2021.4). A dimer
191 of CrSBPase was solvated in a rhombic dodecahedron box with at least 8 Å between the protein
192 atoms and the box edges, which corresponds to ~64000 atoms in total (~18000 water molecules) and
193 a triclinic box of 97x97x68 $Å^3$. The box was neutralized with 18 sodium atoms to make it neutral. The
194 starting conformation was the crystallized structure of oxidized CrSBPase, and we protonated C115
195 and C120 to manually create the reduced state. The protein was described with the Amber14SB force
196 field and water with the TIP3P model. Non-bonding interactions were described with standard
197 parameters: van der Waals interactions had a cut-off of 8 Å, and electrostatic interactions were
198 computed with PME with default parameters with a separation between spaces at 8 Å. Bonds
199 containing a hydrogen atom were restrained with the LINCS algorithm with default parameters. After
200 an energy minimization, the system was equilibrated under the NPT conditions with a δt=1 fs
201 timestep, the velocity-rescale thermostat and the Berendsen barostat. Velocities were generated at
202 100 K and the system was heated up to 300 K in 400 ps before performing 100 ps at 300 K. We then
203 ran simulations of 20 µs under the NPT conditions with a δt=2 fs timestep, the velocity-rescale
204 thermostat and the Parrinello-Rahman barostat.

205

206 **Small-angle X-ray scattering**

207 Pure recombinant *Cr*SBPase was injected on Agilent HPLC BioSEC-3 300 column in buffer A, in line
208 with the X-ray beam capillary at SOLEIL beamline SWING. *Cr*SBPase was untreated or pre-treated
209 with 10 mmol.L^{-1} of reducing agent dithiothreitol (DTTred) or oxidizing agent trans-1,2-dithiane-4,5-
210 diol (DTTox). Diffusion curves were analyzed with ATSAS software to determine the molecular mass
211 and oligomeric state of the protein.

212

213 **Results**

214 **Crystal structure of *Cr*SBPase**

215 Pure recombinant *Cr*SBPase crystallized in space group $P2_12_12$ and provided a complete X-ray
216 diffraction dataset at a resolution of 3.09 Å. The asymmetric unit is composed of six polypeptide
217 chains packing as dimers of dimers (see below) and four water molecules. All chains align within a
218 root mean square deviation (RMSD) <0.25 Å and can be considered identical. Three hundred and
219 nine out of the 331 residues were built in the electron density, the unmodelled sequences are in the
220 disordered extensions at the amino- and carboxy-termini of the model. *Cr*SBPase folds into two
221 distinct domains (figure 1A-B), an amino-terminal domain composed of a mixed β-sheet formed by
222 strands 3-9 and a carboxy-terminal domain composed of a mixed β-sheet formed by strands 10-13.
223 α-helices 1-3 pack on the amino-terminal end of the seven-strand sheet, while α-helices 4,5, and 8
224 pack on the carboxy-terminal end of the four-strand sheet. α-helices 6 and 7 are sandwiched in
225 between the two sheets. A short antiparallel β-sheet is constituted of 4-residue strands 1 and 2
226 separated by a β-turn and preceded by loop A_{113}SCAGTAC_{120}. This motif projects to solvent from α-
227 helices 2 and 3. Residues 113-130 forming the loop and β-hairpin (LBH) motif are positioned away
228 from the core of the protein and will be further discussed in the next sections.

229

230 **CrSBPase catalytic pocket**

231 *Cr*SBPase is structurally similar to its ortholog from the moss *Physcomitrium patens* (Gutle, Roret et
232 al. 2016). SBPase is a homolog of FBPase, another enzyme involved in the CBBC in photosynthetic
233 organisms and also ubiquitously involved in neoglucogenesis. Cytosolic isoforms of FBPase from non-
234 plant sources have been extensively studied (Moorhead, Hodgson et al. 1994, Lee and Hahn 2003).
235 For instance, the crystal structure of human muscle FBPase complexed with its substrate (FBP) was
236 solved (PDB entry: 5l0a, to be published). We aligned the structure *Cr*SBPase onto that of human
237 FBPase:FBP complex, confirming their similarity (RMSD = 0.824 Å) with the notable exception of the
238 LBH motif which is absent in the human enzyme. In a 4-Å distance to FBPase co-crystallized with FBP
239 we aligned 12 residues that are likely available for FBP or SBP binding by *Cr*SBPase (figure 1C): E155,
240 D173, D176, G177, Y287, G289, G290, M291, K317, L318, R319, and E323. These residues are
241 exposed to the solvent in a continuous surface (figure 1D). Water molecule 401 could be modelled at
242 the centre of the putative SBPase catalytic pocket, in the vicinity of E155, D173, D176, R319, and
243 E323, in the catalytic pocket predicted from alignment with human FBPase bound to FBP. W401
244 specifically is in bonding distance to catalytic residues D178, D181, and E328. W401 is likely to react
245 with the substrate SBP during hydrolysis.

246

247 **Sites of redox post-translational modifications**

248 Ten cysteines could be located in the model. Previous redox-based proteomic studies established
249 that SBPase cysteines 115, 120, 222, 231, 355, and 362 are redox-modified by thioredoxin-dependent
250 dithiol/disulfide exchange (Lemaire, Guillon et al. 2004, Pérez-Pérez, Mauriès et al. 2017), S-
251 glutathionylation on unidentified cysteines (Zaffagnini, Bedhomme et al. 2012), or S-nitrosylation at
252 C355 and C362 (Morisse, Zaffagnini et al. 2014). C222, C231, C355, and C362 are putative targets of
253 thioredoxin. DTNB-based thiol titration on the native purified SBPase indicates that 4.0 ± 0.6
254 cysteines are likely reactive owing to their relative exposure to solvent in a free thiol form. Amino
255 acid residue accessible surface area and accessibility (ASA) calculation is consistent with DTNB

256 titration, with C149, C153, C231, and C355 exposed to the solvent (ASA respective areas: 0.154 Å²,
257 0.113 Å², 0.308 Å², and 10.083 Å²), and the six others either shielded from solvent (C169, C222, C340,
258 and C362) or engaged in a disulfide bridge (C115, C120) (Ahmad, Gromiha et al. 2004). In *Cr*SBPase
259 crystal structure, C222 and C231 are positioned on neighbouring strands of the amino-terminal
260 domain, exposing their thiol 3.5 Å away from each other (Figure 1E). The formation of an
261 intramolecular disulfide bridge at this cysteines pair is possible if local main chain rearrangements
262 allow a closer contact. C362 thiol is positioned 10.5 Å away from the nearest thiol group of C340.
263 Additionally, C340 and C362 are exposed on an opposite side of the carboxy-terminal β-sheet,
264 disfavouring the formation of an internal disulfide bridge. C355 points its side chain towards C153
265 and C169 with a thiol-thiol distance of 4.6 Å and 10.1 Å, respectively. Although not observed in our
266 model, a C355-C153/C169 dithiol-disulfide exchange is thus plausible, as described for plant FBPase
267 (Jacquot, Lopez-Jaramillo et al. 1997). Local rearrangements that occur upon FBPase disulfide
268 reduction causes a larger scale relaxation of the active site required to reach maximal catalytic
269 potential (Chiadmi, Navaza et al. 1999) as kinetically characterized for *Arabidopsis* (Yoshida and
270 Hisabori 2018) and *Nicotiana* enzymes (Zimmer, Swart et al. 2021). In SBPase, the FBPase-type
271 regulatory disulfide is not observed but the C115-C120 bridge in the LBH motif may regulate the
272 enzyme by alternative conformational rearrangements. Indeed, the disulfide-bonded cysteines
273 constrain loop A_{113}SCAGTAC_{120} into a compact lasso conformation that could open into a relaxed
274 conformation hypothetically activating catalysis.
275
276 **Sites of post-translational phosphorylations**
277 *Cr*SBPase was reported to be phosphorylated from algae extracts at residues T112, S114, T118, S123,
278 T310, S311, and T313 (Wagner, Gessner et al. 2006, Werth, McConnell et al. 2017, McConnell, Werth
279 et al. 2018). Consistently with the proximity of these residues in two sectors of the sequence
280 (supplementary figure 2), the candidate modification sites are located in two contiguous regions in
281 the three-dimensional model (figure 1F). T112, S114, T118, and S123 are exposed to the solvent of

282 the amino-terminal domain. The residues belong to or are located nearby the A_{113}SCAGTAC_{120} motif
283 where phosphorylations may cross-signal with redox modifications on C115 and C120. T310, S311,
284 and T313 are located on the other edge of the enzyme, at the solvent exposed tip of the carboxy-
285 terminal domain. Their co-localization at the T_{310}SPT_{313} motif likely facilitates a coordinated
286 phosphorylation of the three residues by the same kinase. Because both groups of potential
287 phospho-sites are located at 17-18 Å from the catalytic pocket (H_2O 401 taken as a reference point),
288 there is no straightforward mechanism by which such modifications would exert a control over
289 *Cr*SBPase activity. Analysis of phospho-mimicking mutants along with the identification of the actual
290 kinases/phosphatases couples that control SBPase phosphorylation state would allow to
291 comprehend the role of this putative regulatory mechanism.
292
293 ***Cr*SBPase enzymatic activity**
294 Recombinant *Cr*SBPase was assayed for its capacity to catalyze FBP hydrolysis into F6P (Gutle, Roret
295 et al. 2016), a proxy for the hydrolysis of SBP into S7P that we could not test by lack of available
296 substrate and kinetic reporter method. Previous studies demonstrated that plant SBPase requires the
297 cofactor Mg^{2+} and a chemical reductant (DTT) to be fully activated *in vitro* (Anderson 1974, Woodrow
298 and Walker 1980, Cadet and Meunier 1988). In agreement with this, we found a total absence of
299 activity in the untreated CrSBPase (data not shown), whereas pre-incubation of the enzyme with DTT
300 and Mg^{2+} resulted in a strong activation (figure 2). By testing different concentrations of $MgSO_4$ (3,
301 10, 15, and 20 mM) and DTT (1, 10, 25, 50, and 100 mM), we established that 10 mM of DTT and 10
302 mM $MgSO_4$ are the optimal condition to attain the maximum specific activity which corresponds to
303 12.2 ± 2.2 µmol(NADPH) min^{-1} mg(SBPase)$^{-1}$ (figure 2A and 2B). Unexpectedly, DTT concentrations
304 above 10 mM had an inhibitory effect, causing a drastic drop in activity that probably resulted from
305 structural effects leading to denaturation or aggregation of the enzyme (figure 2A). In contrast, we
306 observed no such inhibitory effect in the presence of magnesium at concentrations above 10 mM
307 (figure 2B). Under physiological conditions, the light-dependent redox regulation of plant SBPase is

308 specifically exerted by f-class thioredoxins (Gutle, Roret et al. 2016), which are reduced by the
309 ferredoxin-thioredoxin cascade (Schürmann and Buchanan 1975). The chloroplast TRX-f2 from
310 Chlamydomonas was thus tested and validated for its capacity to activate CrSBPase by reduction
311 (figure 2C). The maximum activity, corresponding to 12.2 ± 2.2 µmol(NADPH) min-1 mg(SBPase)-1,
312 was obtained by pre-incubating the enzyme with 1 µM CrTRX-f2 supplemented with 1 mM DTT and
313 10 mM $MgSO_4$, and maintained even at higher CrTRX-f2 concentrations (*i.e.*, 5 and 10 µM) (figure
314 2C).
315
316 **Redox controlled dynamics of *Cr*SBPase**
317 *Cr*SBPase crystallized under reducing treatment (10 mmol.L^{-1} TCEP). Among the eight subunits in the
318 asymmetric unit, C115-C120 disulfide is absent in two chains (subunits C coloured in magenta and E
319 coloured in salmon, figure 3D and 3F), while the other six subunits still have the C115-C120 disulfide
320 bridge (figure 3B,C,E,G,H,I). All other cysteines are unaffected by the reducing treatment. These six
321 subunits present mildly variable conformations of the A_{113}SCAGTAC_{120} lasso conformation similar to
322 the untreated oxidized structure of *Cr*SBPase (figure 3A). Reduction of the C115-C120 disulfide
323 increases local disorder (supplementary figure 3), and the main chain electron density became
324 uninterpretable over a few residues for subunits C (residues 115-118, 124-127), and E (residues 119-
325 127).
326 Molecular dynamics (MD) simulations of the reduced structure were performed by starting from a
327 dimer of the crystallized oxidized form and forcing residues C115 and C120 to be reduced in a thiol
328 state (-SH). We then ran two independent replicas of 20 µs of MD. In addition, we also ran two
329 independent replicas of 2 µs of MD in the oxidized form. In one of the replicas of the reduced form
330 (MD1), the protein structure barely changed as observed in the SG(C115)/SG(C120) distance that
331 plateaued at ~7 Å, as well as in the RMSD with respect to the starting conformation that stayed
332 around 2 Å (see supplementary figures 7-8 for plots and 12 for images of the structures). However, in
333 the other replica of the reduced form (MD2), significant changes of conformation appeared: the

334 SG(C115)/SG(C120) distance ended up at ~10 Å with peaks at 20 Å and the RMSD ended up at 3.7
335 and 2.8 Å (supplementary figures 7-8). The difference between MD1 and MD2 is stronger when one
336 focuses on the RMSD of the mobile motif (residues 112 to 131, supplementary figure 9). We
337 observed that after 17 µs of MD all chains adopted an equilibrated conformation and then fluctuated
338 around that conformation (supplementary figure 9); representative structures extracted from MD
339 were thus obtained from a clustering on the time frame (or block) 17-20 µs.
340 The two chains A and B from MD2 adopt a different final conformation (see figure 4A for the overlap
341 with the crystallized oxidized structure and figure 4B for the overlap with the crystallized reduced
342 structure), and we cannot directly conclude on which one is the most stable. Moreover, the residues
343 115 to 128 of each chain from MD1/2 do not overlap well with the crystallized reduced structure
344 which means that neither of the two chains conformations from MD simulations has converged
345 towards the crystallized state. However, we can observe in the reduced crystallized structure that
346 residues 134-148 form an α-helix which is also present in chain B from MD2 whereas this structure is
347 not kept in chain A from MD2 (see green chain on the right of figures 4A-B). In addition, mobile motif
348 from chain B seems to open towards the solvent in a similar way with what was observed for FBPase
349 in the reduced state. Thus, we conclude that chain B from MD2 is more representative of the true
350 reduced conformation than chain A from MD2. If we compare the mobility of chain B from MD2 in
351 the reduced state with one chain in the oxidized state (also chain B from MD2), we can see that the
352 mobile motif is overall more flexible in the reduced state, which is especially true for residues around
353 C120 (residues 118 to 123, supplementary figure 10). We then analyzed the RMSD of residues 112 to
354 131 from chain B during MD2 (supplementary figure 11): residues 112, 130 and 131 barely move
355 which is expected since they belong or are directly connected to the two α-helixes flanking the
356 mobile motif. At ~6 µs of the trajectory almost all other residues (with the exception of C120) display
357 an abrupt change of conformation, with a different magnitude though: starting from ~2 Å, the RMSD
358 jumped to 3 Å for some residues and to 15 Å for other residues (supplementary figures 8, 9, and 11).
359 At ~13.5 µs, another change occurs which involves C120 but not all the other residues. Thus, we

360 conclude that the opening of the motif happens in a concerted way and not sequentially residue per
361 residue.
362
363 **Oligomeric states of *Cr*SBPase**
364 Size-exclusion profile of the purified native protein is polydisperse with at least three distinct species
365 of *Cr*SBPase (supplementary figure 1A,C). Notably, we observed that the protein elutes as a main
366 peak of 79 kDa, close to the mass of a homodimer (theoretical mass from monomer sequence:
367 36,176.7 Da). This peak is broadened by a later-eluting shoulder, with the apparent molecular mass
368 of the tailing species at 48 kDa suggesting the presence of a monomeric state of *Cr*SBPase. The third
369 species elutes at an apparent molecular mass of 145 kDa, that fits with a homotetramer. According
370 to the absorbance of each peak and considering that they represent all states of purified and oxidized
371 *Cr*SBPase in solution, we estimate a repartition of species of 10:53:37 for the
372 tetramer:dimer:monomer mixture (total = 100). Re-injection of the dimer peak fraction over size-
373 exclusion chromatography yielded a similar mixed profile, supporting a dynamic equilibrium over the
374 time of the experiment (>2 h) (data not shown).
375 *Cr*SBPase was crystallized in space groups $P2_12_12$ or $P12_11$ with respectively 6 and 8 protomers in the
376 asymmetric unit. Proteins Interfaces Structures and Assemblies (PISA) analysis reveals that
377 protomers of both crystals pack as homodimers with extensive subunit interface of 4 200 Å² in a
378 similar manner (figure 4A) (Krissinel and Henrick 2007). In the asymmetric unit of CrSBPase
379 crystallized in reducing conditions (7zuv) or within crystallographic neighbouring units of CrSBPase in
380 oxidized state (7b2o), *Cr*SBPase further packs into a homotetramer, a dimer of dimers (figure 4B).
381 The apparent molecular mass of SBPase extracted from *Chlamydomonas* cultures cultivated in TAP
382 medium under 40 $\mu E.m^{-2}.s^{-1}$ illumination is comprised between 130 and 40 kDa with the homodimer
383 representing the predominant state as supported by immunoblot analysis (supplementary figure 4).
384 To further investigate the oligomeric dynamics of CrSBPase, we performed small-angle X-ray
385 scattering (SAXS) analysis of untreated or reduced enzyme *in vitro* which reveals an increase in the

386 protein radius of gyration from 39 to 62 Å upon reduction (supplementary figure 5). This observation
387 implies a change in the oligomeric state of CrSBPase correlating with the redox state. Besides, after a
388 week at 4 °C, the purified protein partially precipitates into an amorphous aggregate that treatment
389 with 10 mmol.L^{-1} TCEP turns into liquid-liquid phase separations (supplementary figure 6). Since the
390 LBH redox module is positioned at the homodimer interface (figure 5C), we postulated that the
391 reduction of the C115-C120 disulfide bond and the subsequent local conformation changes depicted
392 by MD affect the oligomer equilibrium of the enzyme. As a matter of fact, we observed that protein
393 mutants C115S or C120S, which are unable to form the C115-C120 disulfide bond, elute in a different
394 oligomer ratio than wild-type CrSBPase (supplementary figure 1C). Indeed, we observed a relative
395 accumulation of monomer and tetramer species at the expense of the dimer state in both mutants.
396 This suggests that C115-C120 is involved in the stabilization of the dimer. Meanwhile, the activity of
397 the two Cys mutants still responded to DTT/Mg-dependent activation resembling the response of the
398 wild-type protein. No activity was detected for native and untreated forms, while specific activities of
399 C115S and C120S mutants upon treatment with DTT and $MgSO_4$ were respectively 96% and 107%
400 with respect to wild-type maximum activity (13.3 ± 2.5 and 14,9 ± 0,9 µmol(NADPH) min^{-1}
401 mg(SBPase)$^{-1}$ for C115S and C120S mutants, respectively). Based on these data, we can thus conclude
402 that C115-C120 disulfide bond is not the sole thiol-dependent regulatory mechanism involved in the
403 modulation of CrSBPase activity and that the redox dependency of CrSBPase catalysis likely depends
404 on other cysteine pairs. Future studies are required to shed light on the identity of cysteine residues
405 that contribute to CrSBPase catalytic modulation other than C115 and C120.
406

407 **Conclusions and perspectives**

408 We report the first crystal structure of an SBPase from the microalga *Chlamydomonas reinhardtii*, a
409 model for the molecular and cell biology of plants. SBPase is a photosynthetic enzyme involved in the
410 regenerative phase of the CBBC cycle proved to be the target of multiple regulations that we map
411 onto our structural model. The native folding of CrSBPase proved to be highly similar to that of

412 SBPase from the moss *Physcomitrium patens* and to FBPase from chloroplast or cytoplasmic origins.
413 Notwithstanding its propensity to form crystals, recombinant CrSBPase encompasses a range of
414 oligomeric states, dominated by a homodimeric form susceptible to exchange for monomers,
415 tetramers and higher-order assemblies. This oligomer equilibrium is dynamic and correlates with the
416 presence of a disulfide bridge at the vicinity of the monomer-monomer interface, in the SBPase-
417 specific LBH motif. We postulate that the reversible reduction/oxidation of the C115-C120 pair
418 modulates the oligomerization of CrSBPase, through the induction of a local disorder that we
419 observed in the crystal structure of the protein under reducing conditions and that correlates with
420 computations of molecular dynamics.
421 How this oligomeric exchange impacts the actual activity of the enzyme is an open question but
422 should be aligned with previous reports on the allosteric character of the structurally similar FBPase
423 enzyme which follows dimer/tetramer exchanges (Barciszewski, Wisniewski et al. 2016) with a Hill
424 cooperativity coefficient close to 2 representing positive cooperativity in the context of a homodimer
425 (Giudici-Orticoni, Buc et al. 1990). Lastly, systematic proteome mapping in the chloroplast of
426 *Chlamydomonas* localized SBPase in a region surrounding the Rubisco pyrenoid nearby five other
427 CBBC enzymes: phosphoglycerate kinase 1 (PGK), glyceraldehyde-3-phosphate dehydrogenases
428 (GAP1, GAP3), fructose-bisphosphate aldolase (FBA3), ribulose-5-phosphate 3-epimerase (RPE1), and
429 phosphoribulokinase (PRK) (Wang, Patena et al. 2022). Based on our structure-function study on
430 recombinant SBPase, we can hypothesize that upon reductive activation SBPase is co-addressed to
431 this liquid partition of the stroma where it contributes to CBBC reactions at optimized rates.
432

433 **Tables.**

434 Table 1. Crystallographic data collections and models building statistics.

	7b2o (oxidized)	7zuv (partially reduced)
Wavelength (Å)	0.9801	0.9801
Resolution range (Å)	46.62 - 3.095 (3.206 - 3.095)	48.54 - 3.11 (3.221 - 3.11)
Space group	P 2_1 2_1 2	P 1 2_1 1
Unit cell (Å, °)	178.224 183.652 75.196 90 90 90	53.774 163.462 172.765 90 91.939 90
Total reflections	615155 (55989)	376091 (32376)
Unique reflections	45740 (4245)	53456 (5213)
Multiplicity	13.4 (12.9)	7.0 (6.2)
Completeness (%)	99.34 (94.20)	99.65 (97.17)
Mean I/sigma(I)	12.02 (1.72)	8.54 (1.30)
Wilson B-factor (Å^2)	64.82	68.45
R-merge	0.495 (1.877)	0.2492 (1.502)
R-meas	0.5144 (1.954)	0.2691 (1.64)
R-pim	0.1386 (0.5343)	0.1009 (0.6477)
CC1/2	0.983 (0.623)	0.988 (0.479)
CC*	0.996 (0.876)	0.997 (0.805)
Reflections used in refinement	45607 (4242)	53417 (5193)
Reflections used for R-free	1986 (183)	1983 (191)
R-work	0.1942 (0.3071)	0.1963 (0.3239)
R-free	0.2390 (0.3482)	0.2328 (0.3740)
CC(work)	0.944 (0.788)	0.956 (0.726)
CC(free)	0.912 (0.649)	0.949 (0.596)
Number of non-hydrogen atoms	14194	18714
Macromolecules	14190	18704
Solvent	4	10
Protein residues	1859	2451
RMS(bonds) (Å)	0.005	0.004
RMS(angles) (°)	0.75	0.73
Ramachandran favored (%)	94.26	94.80
Ramachandran allowed (%)	5.52	4.70
Ramachandran outliers (%)	0.22	0.50
Rotamer outliers (%)	0.13	0.55
Clashscore	4.88	6.60
Average B-factor (Å^2)	67.00	68.41
macromolecules (Å^2)	67.01	68.40
solvent (Å^2)	49.59	94.37

435 Statistics for the highest-resolution shell are shown in parentheses.

436

437 **Figures legends**

438 **Figure 1. Crystal structure of CrSBPase.**

439 (**A**) Topology is displayed as cartoon with main chain coloured from blue (amino-terminus) to red
440 (carboxy-terminus). (**B**) Rotated view of A. by x-axis over -90°. (**C**) Putative active site residues
441 inferred from alignment with FBPase bound to FBP (5l0a, human muscle fructose-1,6-bisphosphatase
442 E69Q mutant in active R-state in complex with fructose-1,6-bisphosphate) are represented in sticks.
443 (**D**) Surface representation in the B. orientation with putative active site residues coloured in cyan.
444 Water molecule H_2O 401 oxygen is represented as a red sphere. (**E**) Cysteines site chains are
445 represented in spheres. (**F**) Threonines and serines side chains reported to be the target of
446 phosphorylations are represented in spheres.

447

448 **Figure 2. Functional characterization of CrSBPase *in vitro*.**

449 Reported enzymatic activity of CrSBPase assayed for (**A**) reduction by dithiothreitol (DTT), (**B**)
450 Magnesium sulfate ($MgSO_4$), and (**C**) recombinant thioredoxin f2 from *Chlamydomonas reinhardtii*
451 (*Cr*TRX-f2).

452

453 **Figure 3. Crystallographic structures of *Cr*SBPase under reducing treatment.**

454 (**A-I**) Aligned structures of *Cr*SBPase protomers without redox treatment (**A**, 7b2o chain A) or in the
455 presence of 10 mmol.L^{-1} TCEP reducing agent (**B-I**, 7zuv chains A-H).

456

457 **Figure 4. Molecular dynamics simulation of *Cr*SBPase after reduction.**

458 (**A**) Overlap of the crystallographic structure of oxidized SBPase and representative structures of
459 equilibrated reduced SBPase during molecular dynamics simulation 2 (MD2). For structures extracted
460 from MD, only residues 109 to 148 are displayed since most of the other residues are closely
461 overlapping those of the crystallographic structure. (**B**) Overlap of the crystallographic structure of

462 reduced SBPase and representative structures of equilibrated reduced SBPase during MD2. For
463 structures extracted from MD, only residues 109 to 148 are displayed.
464
465 **Figure 5. Oligomeric structure of CrSBPase.**
466 (**A**) Asymmetric unit dimer of untreated *Cr*SBPase (7b2o). Chains are represented in cartoon and
467 coloured cyan (chain B) and salmon (chain E). (**B**) Asymmetric unit homotetramer under reducing
468 treatment (7zuv). Chains A (cyan), C (magenta), F (white), and H (orange) belong to the same
469 asymmetric unit. (**C**) Close-up view on figure A homodimer interface. Loop 113-ASCAGTAC-120 from
470 chain B (in cyan) is in 5-Å distance of neighbouring chain E (in salmon). C115 and C120 are bonded by
471 a disulfide bridge. (**D**) Surface representation of 7b2o homodimer, coloured according to
472 conservation score from teal (lowest conservation) to purple (highest conservation) among 150
473 aligned homologs.
474
475 ## Supplementary information
476 **Supplementary table 1. Primers used for point mutagenesis.**

5'-forward C115S	CCGCACCGCCTCGAGCGCCGGTACCGCCTGCGTG
3'-reverse C115S	CACGCAGGCGGTACCGGCGCTCGAGGCGGTGCGG
5'-forward C120S	GCGCCGGTACCGCCAGCGTGAACAGCTTCGGCG
3'-reverse C120S	CGCCGAAGCTGTTCACGCTGGCGGTACCGGCGC

477

478 **Supplementary figure 1. Purification of recombinant *Cr*SBPase.**

479 A. Size-exclusion chromatography profile recorded at absorbance λ= 280 nm on Superdex 200 26/600
480 GL column. B. Electrophoresis of affinity-chromatography fractions on 12% acrylamide gel in
481 denaturing and reducing condition. Gel was stained with Coomassie blue. Mw: molecular mass
482 standards ladder. C. Size-exclusion chromatograms of *Cr*SBPase wild-type (blue), mutant C115S
483 (orange), mutant C120S (gray).

484

485 **Supplementary figure 2. SBPase multiple sequences alignment.**

486 *Cr*SBPase mature sequence was used for a BLAST search. Retrieved homolog sequences were aligned
487 and coloured-coded according to residue conservation. Illustration made with EndScript (Robert and
488 Gouet 2014).

489

490 **Supplementary figure 3. Related to figure 3. Local disorder of the A_{113}SCAGTAC_{120} loop.**

491 Main chain was traced according to crystallographic b-factor, with large orange sections representing
492 high b-factor values and thin blue sections representing low b-factors. A-I. Aligned structures of
493 *Cr*SBPase protomers without redox treatment (A, 7b2o chain A) or in the presence of 10 $mmol.L^{-1}$
494 TCEP reducing agent (B-I, 7zuv chains A-H).

495

496 **Supplementary figure 4. Size-exclusion fractionation of *Chlamydomonas* cell extracts.**

497 A. *Chlamydomonas* cell culture was harvested, lysed and the soluble fraction of the lysate was loaded
498 on Superose6 16/600 size-exclusion column. Chromatography fractions were analyzed by western
499 blot with anti-*Cr*SBPase primary antibodies. First membrane was loaded with fractions eluted from
500 40 to 80 mL. Second membrane was loaded with fractions eluted from 80 to 120 mL. M lane is
501 loaded with molecular mass standards ladder. Recombinant *Cr*SBPase was loaded on last lane.

502

503 **Supplementary figure 5. Size-exclusion chromatography coupled to small angle X-rays scattering**
504 **(SEC-SAXS) of *Cr*SBPase.**
505 A. X-ray scattering curve log(I) = f(s) for pure *Cr*SBPase untreated (dark blue) or treated (light blue)
506 with 10 mmol.L^{-1} dithiothreitol (DTT). B. Radius of gyration of untreated protein was computed by
507 ATSAS Primus Guinier Wizard as Rg = 39.14 ± 0.06 Å (Franke, Petoukhov et al. 2017). C. Radius of
508 gyration of DTT-treated protein was computed as Rg = 62.47 ± 0.38 Å.
509
510 **Supplementary figure 6. Phase separation of reduced *Cr*SBPase precipitates.**
511 *Cr*SBPase at 2 mg/mL formed amorphous precipitates after storage at 4 °C for a week. The
512 suspension was sedimented by centrifugation at 20,000 *g* for 20 minutes and a microliter drop of the
513 supernatant or of the pellet were treated with 10 mmol.L^{-1} reducing agent TCEP and visualized by
514 binocular optical microscope. A. Untreated precipitate. B. TCEP-treated precipitate. C. Untreated
515 supernatant. D. TCEP-treated supernatant.
516
517 **Supplementary figures 7-11. Computational detail of molecular dynamic simulation.**
518
519 **Supplementary figure 7.**
520 SG(Cys115)/SG(Cys120) distances along the MD trajectories for each chain (left: oxidized state, right:
521 reduced state). Light colours: raw data saved every 100 ps, dark colours: moving average on 20ns
522 blocs.
523
524 **Supplementary figure 8.**
525 RMSD of main chain along the MD trajectories for each chain (left: oxidized state, right: reduced
526 state). Light colours: raw data saved every 100 ps, dark colours: moving average on 20 ns blocs.
527

528 **Supplementary figure 9.**

529 RMSD of main chain of the mobile motif in the reduced state (residues 112 to 131) along the MD
530 trajectories for each chain (left: RMSD with respect to the starting conformation of MD, right: RMSD
531 with respect to the conformation at 20 µs). Light colours: raw data saved every 100 ps, dark colours:
532 moving average on 20 ns blocs.

533

534 **Supplementary figure 10.**

535 RMSF per residue for each chain (top row: full sequence, bottom row: zoom on residues 110 to 170;
536 left column: oxidized state, middle column: reduced state, right column: comparison of one chain
537 from each state).

538

539 **Supplementary figure 11.**

540 RMSD of main chain of each residue from the mobile motif along the trajectory of chain B from MD2.
541 Data are moving average on 200 ns blocs.

542

543 **Supplementary figure 12. Structures of CrSBPase retrieved from molecular dynamics simulations 1**
544 **and 2**.

545 Two independent replicas of 20 µs were performed. In one of them (MD1), the overall structure of
546 both chains of the enzyme barely changed. To illustrate this, we present in supplementary figure 12
547 the overlap between the crystallographic oxidized structure and representative structures extracted
548 from MD (based on clustering the last 3 µs since each chain does not display significative changes
549 after 17 µs). A. Overlap of the crystallographic structure of oxidized CrSBPase and representative
550 structures of equilibrated reduced SBPase during MD1. For structures extracted from MD, only
551 residues 111 to 132 are displayed since the other residues are closely overlapping those of the
552 crystallographic structure. B. Overlap of the crystallographic structure of oxidized SBPase and
553 representative structures of equilibrated reduced CrSBPase during MD2. For structures extracted

554 from MD, only residues 109 to 148 are displayed since most of the other residues are closely
555 overlapping those of the crystallographic structure.
556

557 **Authors contributions**

558 JH, NC: Conceptualization; JH, NC, MS, TLM: Data curation; JH, NC, MZ: Formal analysis; JH: Funding
559 acquisition; JH, NC, MZ, SDL, MS, TLM: Investigation; JH, NC, MZ, MS, TLM: Methodology; JH, SDL:
560 Project administration; JH, NC, SDL: Resources; NC: Software; JH, MZ: Supervision; JH, NC, MZ, SDL,
561 MS, TLM: Writing - original draft; JH, NC, MZ, SDL, MS, TLM: Writing - review & editing.
562

563 **Acknowledgements**

564 We acknowledge the Institut de Biologie Physico-Chimique (CNRS, FR 505) for access to the
565 crystallization facility. We acknowledge SOLEIL for provision of synchrotron radiation facilities at
566 beamlines SWING, PROXIMA-1, and PROXIMA-2A. We thank Guillaume Q. Robert for his contribution
567 to protein purification, crystallization under reducing treatment, and model building. Plasmids pSL-
568 175, -181, and -182 were cloned by Dr. Laure Michelet. This work was funded by the grant
569 CALVINTERACT from the Agence Nationale de la Recherche (ANR-19-CE11-0009). Martina Santoni
570 received funding from the University of Bologna (Bologna, Italy) and Sorbonne University (Paris,
571 France) exchange program ERASMUS+. This work was performed using HPC resources from
572 GENCI–IDRIS (Grant 2021-077156). The authors express their gratitude to the financial support of the
573 AAP AIN INSB CNRS.
574

575 **Conflicts of interest statement**

576 The authors report no conflict of interest relevant to the conduct or report of this research.
577
578

579 **Bibliography**

580 Adams, P. D., P. V. Afonine, G. Bunkóczi, V. B. Chen, N. Echols, J. J. Headd, L. W. Hung, S. Jain, G. J.
581 Kapral, R. W. Grosse Kunstleve, A. J. McCoy, N. W. Moriarty, R. D. Oeffner, R. J. Read, D. C.
582 Richardson, J. S. Richardson, T. C. Terwilliger and P. H. Zwart (2011). "The Phenix software for
583 automated determination of macromolecular structures." Methods **55**(1): 94-106.
584 Ahmad, S., M. Gromiha, H. Fawareh and A. Sarai (2004). "ASAView: database and tool for solvent
585 accessibility representation in proteins." BMC Bioinformatics **5**: 51.
586 Almagro Armenteros, J. J., M. Salvatore, O. Emanuelsson, O. Winther, G. von Heijne, A. Elofsson and
587 H. Nielsen (2019). "Detecting sequence signals in targeting peptides using deep learning." Life Sci
588 Alliance **2**(5).
589 Anderson, L. E. (1974). "Activation of pea leaf chloroplast sedoheptulose 1,7-diphosphate
590 phosphatase by light and dithiothreitol." Biochem Biophys Res Commun **59**(3): 907-913.
591 Barciszewski, J., J. Wisniewski, R. Kolodziejczyk, M. Jaskolski, D. Rakus and A. Dzugaj (2016). "T-to-R
592 switch of muscle fructose-1,6-bisphosphatase involves fundamental changes of secondary and
593 quaternary structure." Acta Crystallogr D Struct Biol **72**(Pt 4): 536-550.
594 Cadet, F. and J. C. Meunier (1988). "pH and kinetic studies of chloroplast sedoheptulose-1,7-
595 bisphosphatase from spinach (Spinacia oleracea)." Biochem J **253**(1): 249-254.
596 Calvin, M. (1962). "The path of carbon in photosynthesis." Science **135**(3507): 879-889.
597 Chiadmi, M., A. Navaza, M. Miginiac-Maslow, J. P. Jacquot and J. Cherfils (1999). "Redox signalling in
598 the chloroplast: structure of oxidized pea fructose-1,6-bisphosphate phosphatase." EMBO J **18**(23):
599 6809-6815.
600 Emanuelsson, O., S. Brunak, G. von Heijne and H. Nielsen (2007). "Locating proteins in the cell using
601 TargetP, SignalP and related tools." Nat Protoc **2**(4): 953-971.
602 Emsley, P., B. Lohkamp, W. G. Scott and K. Cowtan (2010). "Features and development of Coot." Acta
603 Crystallogr D Biol Crystallogr **66**(Pt 4): 486-501.
604 Feng, L., Y. Han, G. Liu, B. An, J. Yang, G. Yang, Y. Li and Y. Zhu (2007). "Overexpression of
605 sedoheptulose-1,7-bisphosphatase enhances photosynthesis and growth under salt stress in
606 transgenic rice plants." Funct Plant Biol **34**(9): 822-834.
607 Feng, L., K. Wang, Y. Li, Y. Tan, J. Kong, H. Li, Y. Li and Y. Zhu (2007). "Overexpression of SBPase
608 enhances photosynthesis against high temperature stress in transgenic rice plants." Plant Cell Rep
609 **26**(9): 1635-1646.
610 Franke, D., M. V. Petoukhov, P. V. Konarev, A. Panjkovich, A. Tuukkanen, H. D. T. Mertens, A. G.
611 Kikhney, N. R. Hajizadeh, J. M. Franklin, C. M. Jeffries and D. I. Svergun (2017). "ATSAS 2.8: a
612 comprehensive data analysis suite for small-angle scattering from macromolecular solutions." J Appl
613 Crystallogr **50**(Pt 4): 1212-1225.
614 Giudici-Orticoni, M. T., J. Buc, M. Bidaud and J. Ricard (1990). "Thermodynamics of information
615 transfer between subunits in oligomeric enzymes and kinetic cooperativity. 3. Information transfer
616 between the subunits of chloroplast fructose bisphosphatase." Eur J Biochem **194**(2): 483-490.
617 Gurrieri, L., A. Del Giudice, N. Demitri, G. Falini, N. V. Pavel, M. Zaffagnini, M. Polentarutti, P. Crozet,
618 C. H. Marchand, J. Henri, P. Trost, S. D. Lemaire, F. Sparla and S. Fermani (2019). "Arabidopsis and
619 Chlamydomonas phosphoribulokinase crystal structures complete the redox structural proteome of
620 the Calvin-Benson cycle." Proc Natl Acad Sci U S A **116**(16): 8048-8053.
621 Gutle, D. D., T. Roret, S. J. Muller, J. Couturier, S. D. Lemaire, A. Hecker, T. Dhalleine, B. B. Buchanan,
622 R. Reski, O. Einsle and J. P. Jacquot (2016). "Chloroplast FBPase and SBPase are thioredoxin-linked
623 enzymes with similar architecture but different evolutionary histories." Proc Natl Acad Sci U S A
624 **113**(24): 6779-6784.
625 Hammel, A., F. Sommer, D. Zimmer, M. Stitt, T. Mühlhaus and M. Schroda (2020). "Overexpression of
626 Sedoheptulose-1,7-Bisphosphatase Enhances Photosynthesis in Chlamydomonas reinhardtii and Has
627 No Effect on the Abundance of Other Calvin-Benson Cycle Enzymes." Front Plant Sci **11**: 868.

628 Jacquot, J. P., J. Lopez-Jaramillo, M. Miginiac-Maslow, S. Lemaire, J. Cherfils, A. Chueca and J. Lopez-
629 Gorge (1997). "Cysteine-153 is required for redox regulation of pea chloroplast fructose-1,6-
630 bisphosphatase." FEBS Lett **401**(2-3): 143-147.
631 Johnson, M. P. (2016). "Photosynthesis." Essays Biochem **60**(3): 255-273.
632 Johnson, X. and J. Alric (2013). "Central carbon metabolism and electron transport in
633 Chlamydomonas reinhardtii: metabolic constraints for carbon partitioning between oil and starch."
634 Eukaryot Cell **12**(6): 776-793.
635 Jumper, J., R. Evans, A. Pritzel, T. Green, M. Figurnov, O. Ronneberger, K. Tunyasuvunakool, R. Bates,
636 A. Zidek, A. Potapenko, A. Bridgland, C. Meyer, S. A. A. Kohl, A. J. Ballard, A. Cowie, B. Romera-
637 Paredes, S. Nikolov, R. Jain, J. Adler, T. Back, S. Petersen, D. Reiman, E. Clancy, M. Zielinski, M.
638 Steinegger, M. Pacholska, T. Berghammer, S. Bodenstein, D. Silver, O. Vinyals, A. W. Senior, K.
639 Kavukcuoglu, P. Kohli and D. Hassabis (2021). "Highly accurate protein structure prediction with
640 AlphaFold." Nature **596**(7873): 583-589.
641 Krissinel, E. and K. Henrick (2007). "Inference of macromolecular assemblies from crystalline state." J
642 Mol Biol **372**(3): 774-797.
643 Kubis, A. and A. Bar-Even (2019). "Synthetic biology approaches for improving photosynthesis." J Exp
644 Bot **70**(5): 1425-1433.
645 Lee, S. W. and T. R. Hahn (2003). "Light-regulated differential expression of pea chloroplast and
646 cytosolic fructose-1,6-bisphosphatases." Plant Cell Rep **21**(6): 611-618.
647 Lefebvre, S., T. Lawson, O. V. Zakhleniuk, J. C. Lloyd, C. A. Raines and M. Fryer (2005). "Increased
648 sedoheptulose-1,7-bisphosphatase activity in transgenic tobacco plants stimulates photosynthesis
649 and growth from an early stage in development." Plant Physiol **138**(1): 451-460.
650 Lemaire, S. D., B. Guillon, P. Le Maréchal, E. Keryer, M. Miginiac-Maslow and P. Decottignies (2004).
651 "New thioredoxin targets in the unicellular photosynthetic eukaryote *Chlamydomonas reinhardtii*."
652 Proc Natl Acad Sci U S A **101**(19): 7475-7480.
653 Lemaire, S. D., D. Tedesco, P. Crozet, L. Michelet, S. Fermani, M. Zaffagnini and J. Henri (2018).
654 "Crystal Structure of Chloroplastic Thioredoxin f2 from Chlamydomonas reinhardtii Reveals Distinct
655 Surface Properties." Antioxidants (Basel) **7**(12).
656 Liebschner, D., P. V. Afonine, M. L. Baker, G. Bunkóczi, V. B. Chen, T. I. Croll, B. Hintze, L. W. Hung, S.
657 Jain, A. J. McCoy, N. W. Moriarty, R. D. Oeffner, B. K. Poon, M. G. Prisant, R. J. Read, J. S. Richardson,
658 D. C. Richardson, M. D. Sammito, O. V. Sobolev, D. H. Stockwell, T. C. Terwilliger, A. G. Urzhumtsev, L.
659 L. Videau, C. J. Williams and P. D. Adams (2019). "Macromolecular structure determination using X-
660 rays, neutrons and electrons: recent developments in Phenix." Acta Crystallogr D Struct Biol **75**(Pt
661 10): 861-877.
662 McConnell, E. W., E. G. Werth and L. M. Hicks (2018). "The phosphorylated redox proteome of
663 Chlamydomonas reinhardtii: Revealing novel means for regulation of protein structure and function."
664 Redox Biol **17**: 35-46.
665 Mettler, T., T. Muhlhaus, D. Hemme, M. A. Schottler, J. Rupprecht, A. Idoine, D. Veyel, S. K. Pal, L.
666 Yaneva-Roder, F. V. Winck, F. Sommer, D. Vosloh, B. Seiwert, A. Erban, A. Burgos, S. Arvidsson, S.
667 Schonfelder, A. Arnold, M. Gunther, U. Krause, M. Lohse, J. Kopka, Z. Nikoloski, B. Mueller-Roeber, L.
668 Willmitzer, R. Bock, M. Schroda and M. Stitt (2014). "Systems Analysis of the Response of
669 Photosynthesis, Metabolism, and Growth to an Increase in Irradiance in the Photosynthetic Model
670 Organism Chlamydomonas reinhardtii." Plant Cell **26**(6): 2310-2350.
671 Moorhead, G. B., R. J. Hodgson and W. C. Plaxton (1994). "Copurification of cytosolic fructose-1,6-
672 bisphosphatase and cytosolic aldolase from endosperm of germinating castor oil seeds." Arch
673 Biochem Biophys **312**(2): 326-335.
674 Morisse, S., M. Zaffagnini, X. H. Gao, S. D. Lemaire and C. H. Marchand (2014). "Insight into protein S-
675 nitrosylation in Chlamydomonas reinhardtii." Antioxid Redox Signal **21**(9): 1271-1284.
676 Nishizawa, A. N. and B. B. Buchanan (1981). "Enzyme regulation in C4 photosynthesis. Purification
677 and properties of thioredoxin-linked fructose bisphosphatase and sedoheptulose bisphosphatase
678 from corn leaves." J Biol Chem **256**(12): 6119-6126.

679 Ohta, J. (2022). "A novel variant of the Calvin-Benson cycle bypassing fructose bisphosphate." Sci Rep
680 **12**(1): 3984.
681 Pérez-Pérez, M. E., A. Mauriès, A. Maes, N. J. Tourasse, M. Hamon, S. D. Lemaire and C. H. Marchand
682 (2017). "The Deep Thioredoxome in Chlamydomonas reinhardtii: New Insights into Redox
683 Regulation." Mol Plant **10**(8): 1107-1125.
684 Robert, X. and P. Gouet (2014). "Deciphering key features in protein structures with the new
685 ENDscript server." Nucleic Acids Research **42**(W1): W320-W324.
686 Rosenthal, D. M., A. M. Locke, M. Khozaei, C. A. Raines, S. P. Long and D. R. Ort (2011). "Over-
687 expressing the C(3) photosynthesis cycle enzyme Sedoheptulose-1-7 Bisphosphatase improves
688 photosynthetic carbon gain and yield under fully open air CO(2) fumigation (FACE)." BMC Plant Biol
689 **11**: 123.
690 Schmollinger, S., T. Mühlhaus, N. R. Boyle, I. K. Blaby, D. Casero, T. Mettler, J. L. Moseley, J. Kropat, F.
691 Sommer, D. Strenkert, D. Hemme, M. Pellegrini, A. R. Grossman, M. Stitt, M. Schroda and S. S.
692 Merchant (2014). "Nitrogen-Sparing Mechanisms in Chlamydomonas Affect the Transcriptome, the
693 Proteome, and Photosynthetic Metabolism." Plant Cell **26**(4): 1410-1435.
694 Schürmann, P. and B. B. Buchanan (1975). "Role of ferredoxin in the activation of sedoheptulose
695 diphosphatase in isolated chloroplasts." Biochim Biophys Acta **376**(1): 189-192.
696 Simkin, A. J., P. E. Lopez-Calcagno, P. A. Davey, L. R. Headland, T. Lawson, S. Timm, H. Bauwe and C.
697 A. Raines (2017). "Simultaneous stimulation of sedoheptulose 1,7-bisphosphatase, fructose 1,6-
698 bisphophate aldolase and the photorespiratory glycine decarboxylase-H protein increases CO(2)
699 assimilation, vegetative biomass and seed yield in Arabidopsis." Plant Biotechnol J **15**(7): 805-816.
700 Wagner, V., G. Gessner, I. Heiland, M. Kaminski, S. Hawat, K. Scheffler and M. Mittag (2006).
701 "Analysis of the phosphoproteome of Chlamydomonas reinhardtii provides new insights into various
702 cellular pathways." Eukaryot Cell **5**(3): 457-468.
703 Wang, L., W. Patena, K. A. Van Baalen, Y. Xie, E. R. Singer, S. Gavrilenko, M. Warren-Williams, L. Han,
704 H. R. Harrigan, V. Chen, V. T. N. P. Ton, S. Kyin, H. H. Shwe, M. H. Cahn, A. T. Wilson, J. Hu, D. J.
705 Schnell, C. D. McWhite and M. Jonikas (2022). "A Chloroplast Protein Atlas Reveals Novel Structures
706 and Spatial Organization of Biosynthetic Pathways." bioRxiv: 2022.2005.2031.493820.
707 Werth, E. G., E. W. McConnell, T. S. Gilbert, I. Couso Lianez, C. A. Perez, C. K. Manley, L. M. Graves, J.
708 G. Umen and L. M. Hicks (2017). "Probing the global kinome and phosphoproteome in
709 Chlamydomonas reinhardtii via sequential enrichment and quantitative proteomics." Plant J **89**(2):
710 416-426.
711 Wilson, R. H., M. Hayer-Hartl and A. Bracher (2019). "Crystal structure of phosphoribulokinase from
712 Synechococcus sp. strain PCC 6301." Acta Crystallogr F Struct Biol Commun **75**(Pt 4): 278-289.
713 Woodrow, I. E. (1982). "Sedoheptulose-1,7-bisphosphatase from wheat chloroplasts." Methods
714 Enzymol **90 Pt E**: 392-396.
715 Woodrow, I. E. and D. A. Walker (1980). "Light-mediated activation of stromal sedoheptulose
716 bisphosphatase." Biochem J **191**(3): 845-849.
717 Yoshida, K. and T. Hisabori (2018). "Determining the Rate-Limiting Step for Light-Responsive Redox
718 Regulation in Chloroplasts." Antioxidants (Basel) **7**(11).
719 Zaffagnini, M., M. Bedhomme, C. H. Marchand, S. Morisse, P. Trost and S. D. Lemaire (2012). "Redox
720 regulation in photosynthetic organisms: focus on glutathionylation." Antioxid Redox Signal **16**(6):
721 567-586.
722 Zimmer, D., C. Swart, A. Graf, S. Arrivault, M. Tillich, S. Proost, Z. Nikoloski, M. Stitt, R. Bock, T.
723 Mühlhaus and A. Boulouis (2021). "Topology of the redox network during induction of
724 photosynthesis as revealed by time-resolved proteomics in tobacco." Sci Adv **7**(51): eabi8307.
725

Figure 1.

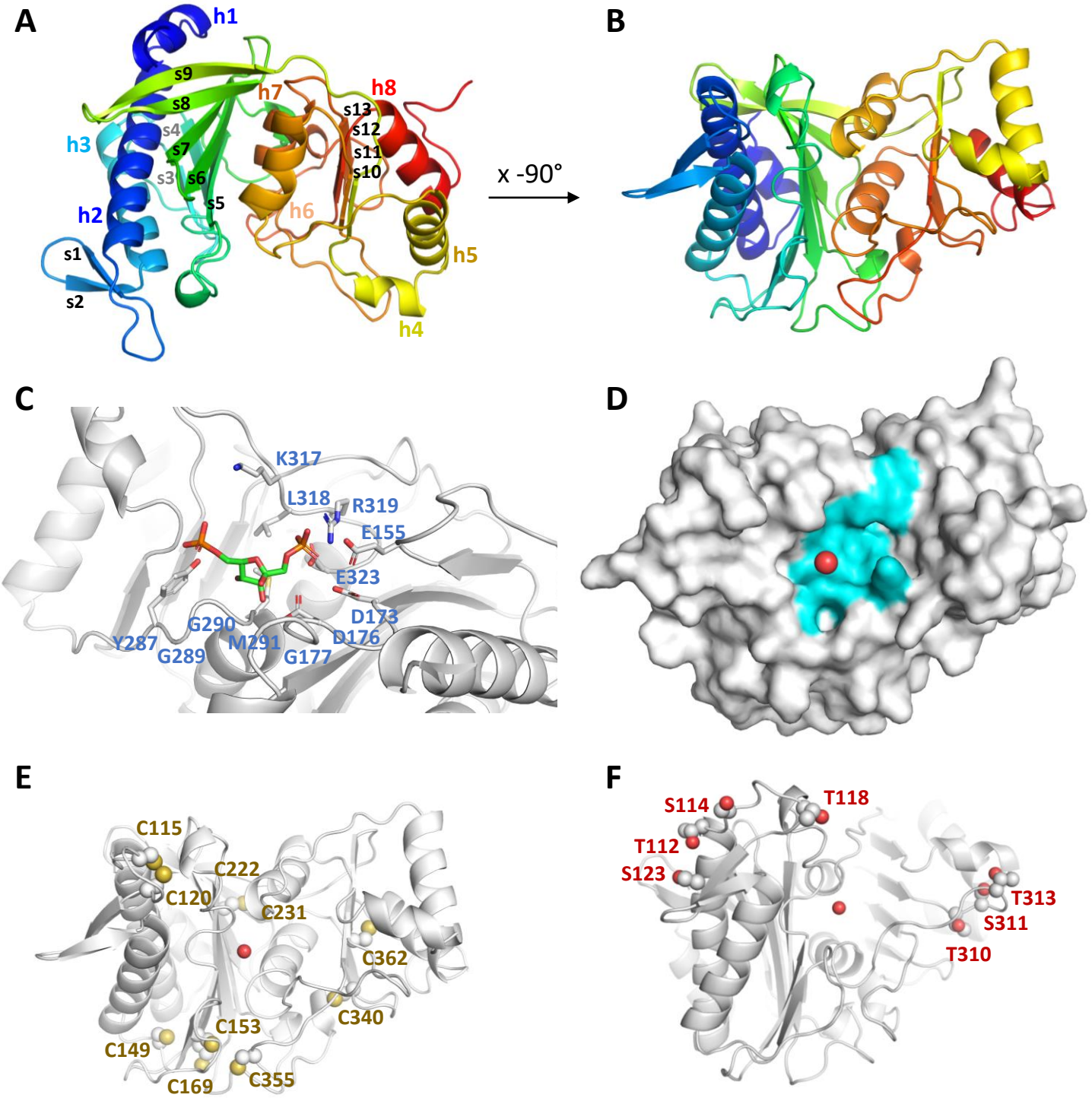
A
h1
s9
s8
h7
h8
s13
s12
s11
s10
h3
s4
s7
s3
s6
s5
h2
h6
s1
s2
h5
h4
x -90°
B
C
K317
L318
R319
E155
E323
D173
G290
D176
Y287
M291
G289
G177
D
E
C115
C222
C120
C231
C362
C340
C153
C149
C169
C355
F
S114
T118
T112
S123
T313
S311
T310

Figure 2.

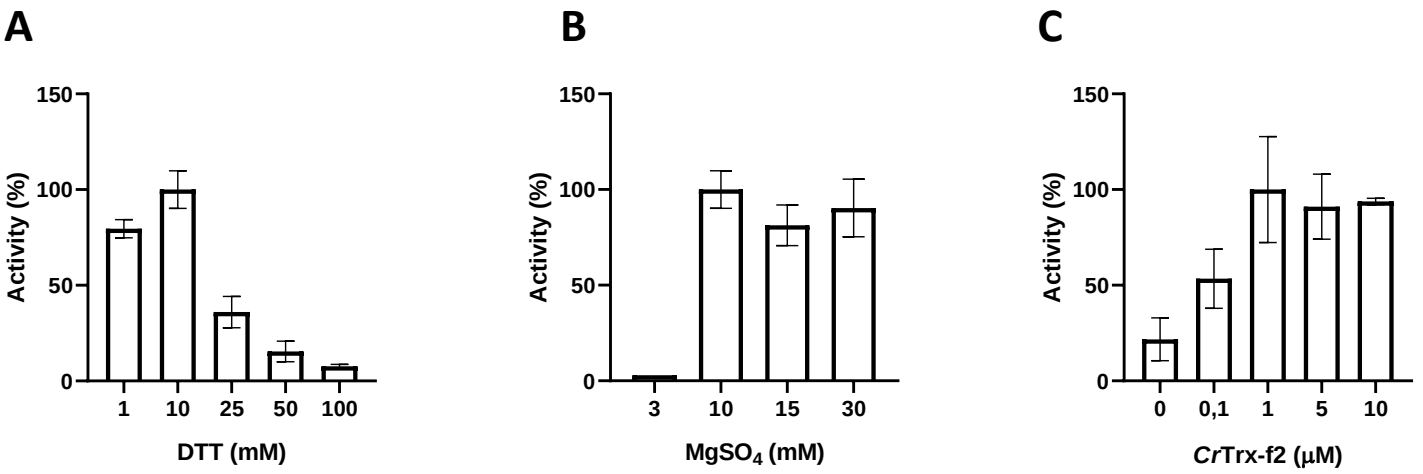
A
B
C
150
100
50
0
Activity (%)
1
10
25
50
100
DTT (mM)
3
10
15
30
MgSO4 (mM)
0
0,1
1
5
10
CrTrx-f2 (µM)

Figure 3.

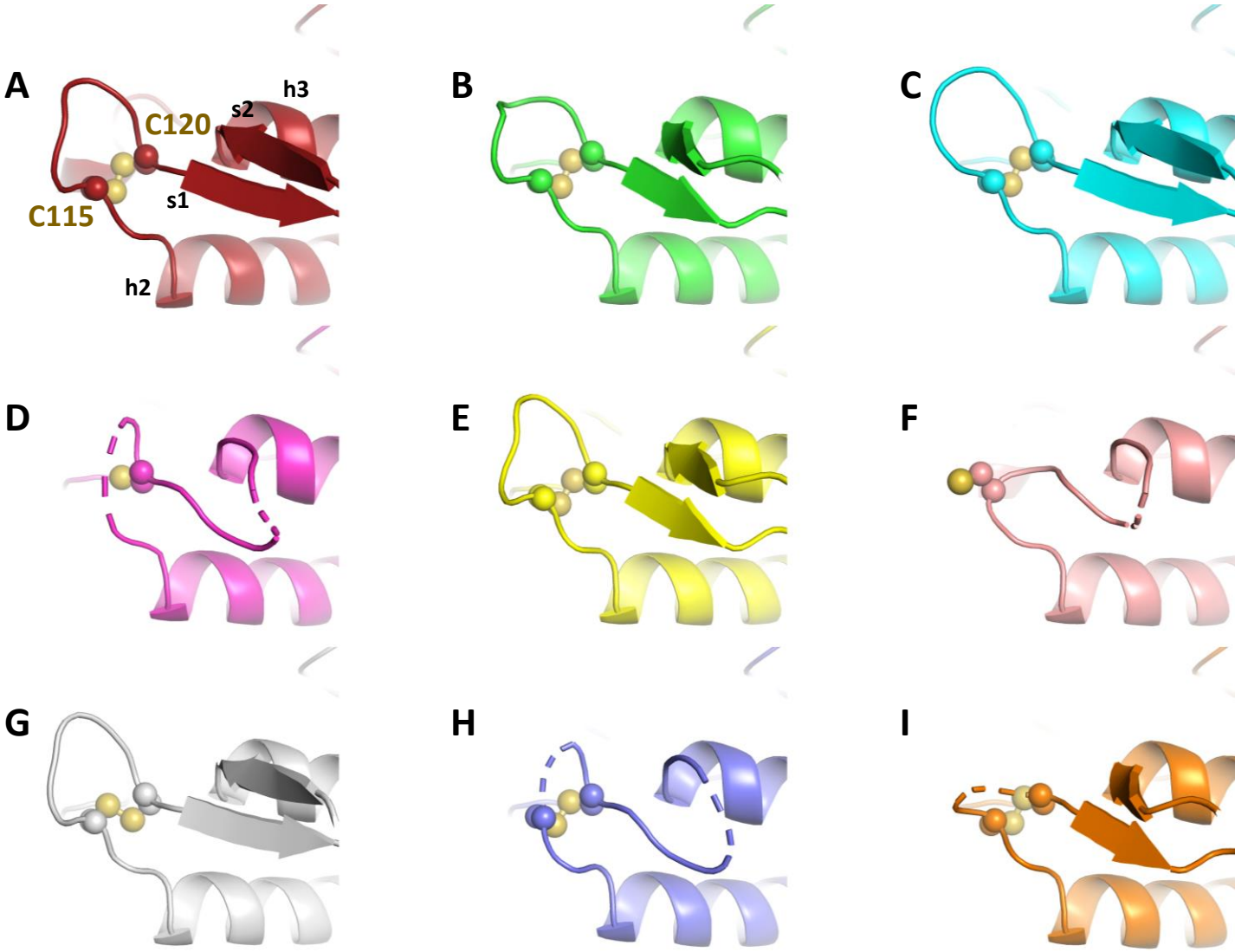

Figure 4.

A

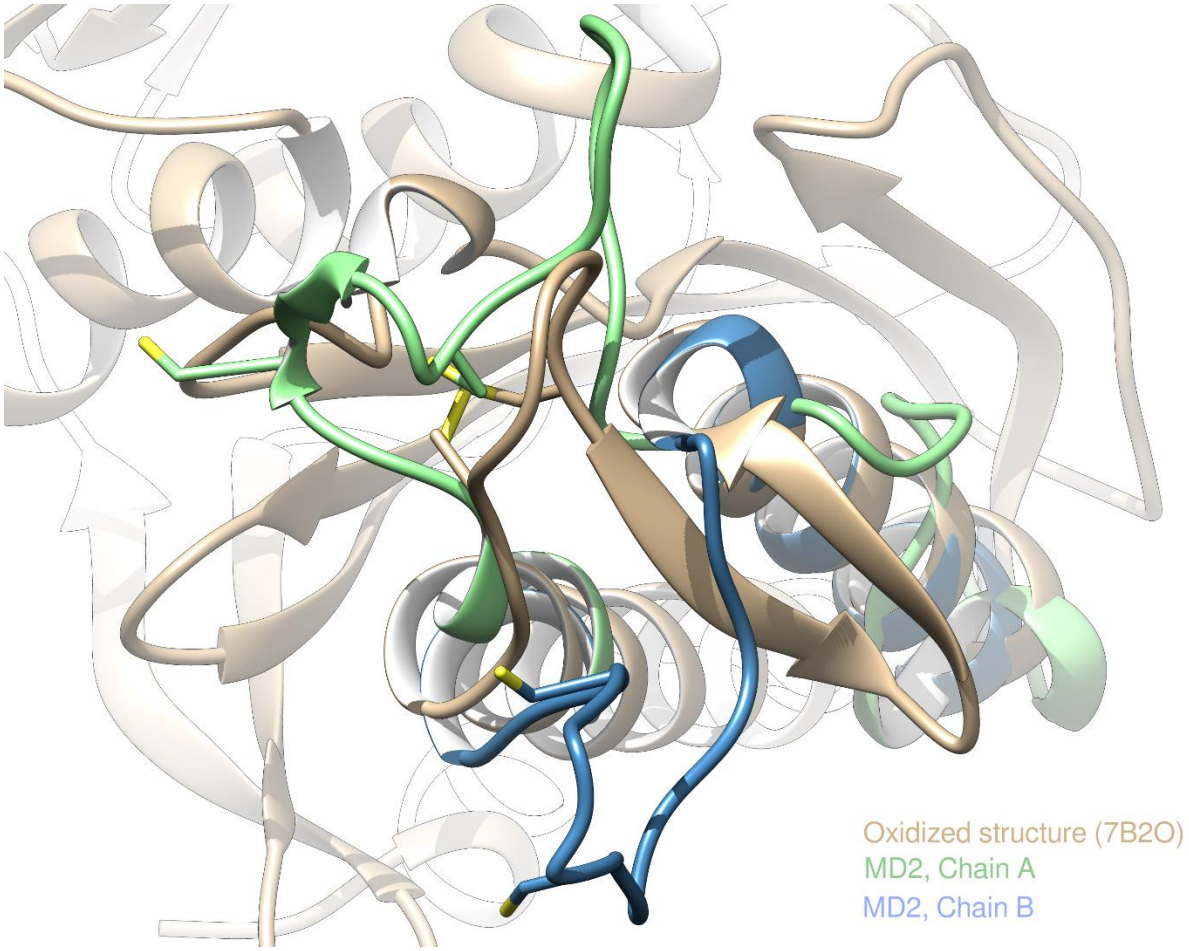
Oxidized structure (7B2O)
MD2, Chain A
MD2, Chain B

B

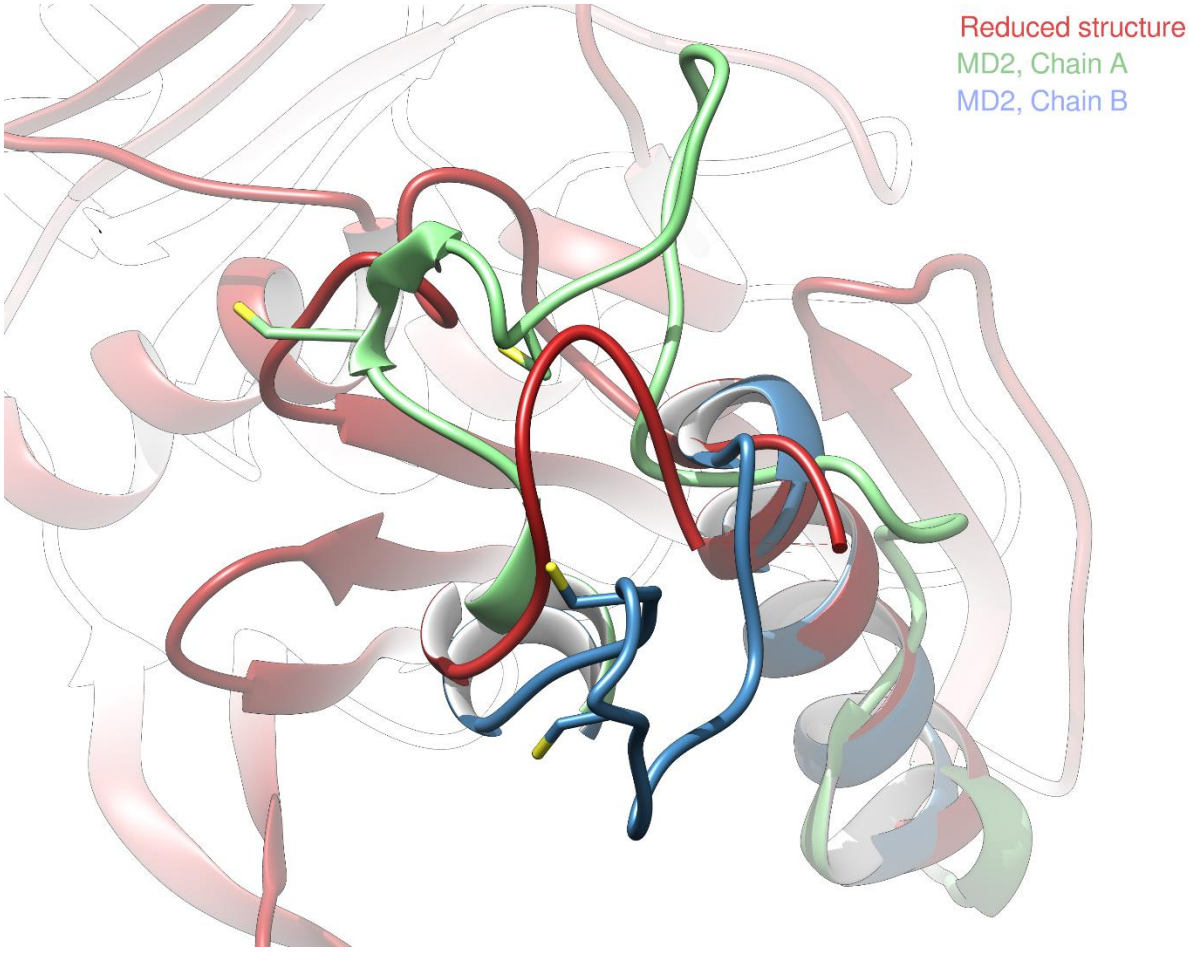
Reduced structure
MD2, Chain A
MD2, Chain B
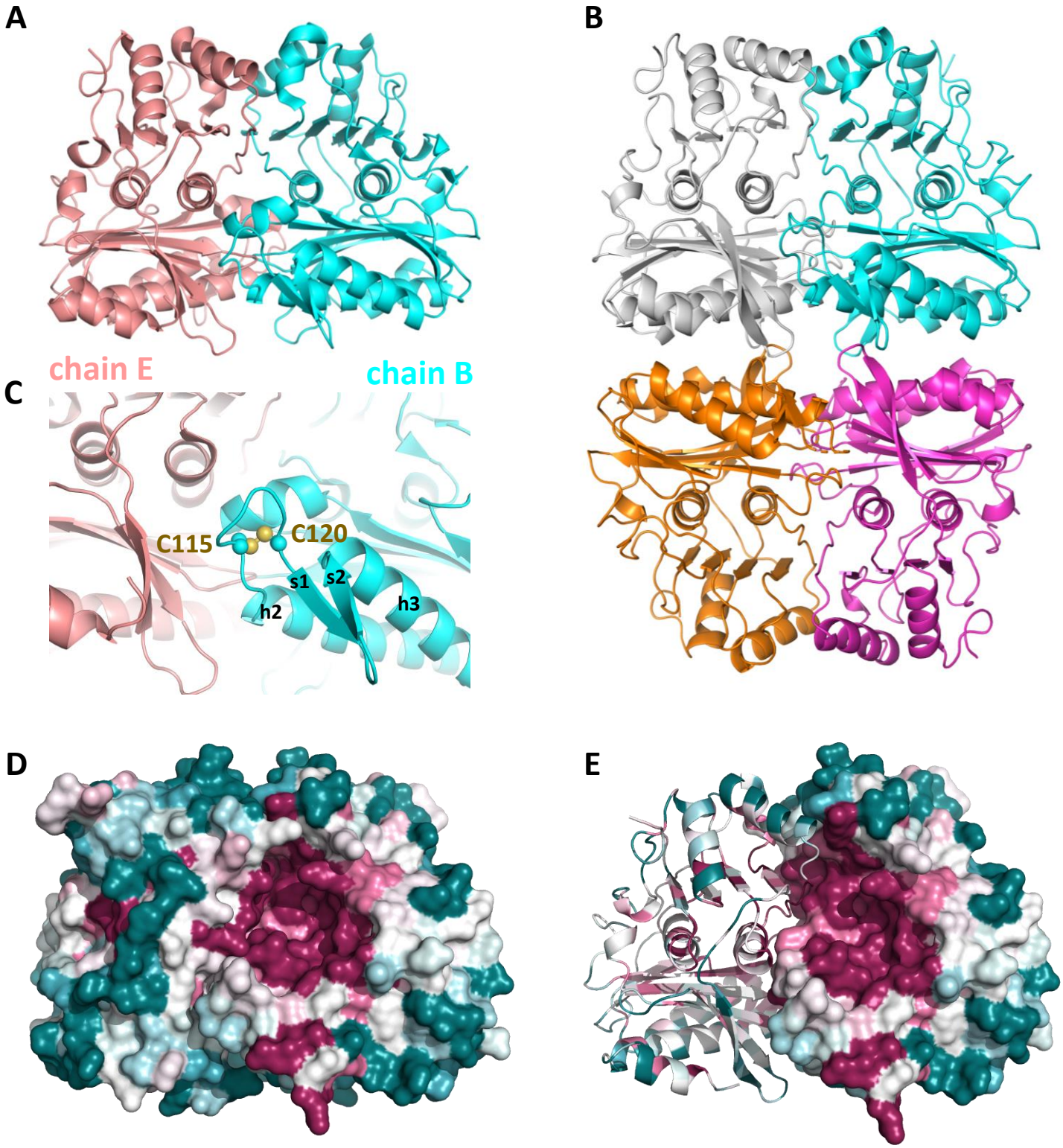
Figure 5.